Department of Physics and Astronomy
Heidelberg University

Bachelor Thesis in Physics
submitted by

Jan Raymond Dumke

born in Köln (Germany)

2000

Exploring the Heat and Pull Method for Fabricating Adiabatic Couplers

This Bachelor Thesis has been carried out by Jan Dumke at the
Kirchhoff Institute for Physics in Heidelberg
under the supervision of
Prof. Dr. rer. nat. Wolfram Pernice

Abstract

english version below Die Arbeit wurde in Englisch verfasst. Quantencomputer auf Basis integrierter photonischer Plattformen benötigen oft eine Möglichkeit, Photonen verlustfrei zwischen der integrierten photonischen Plattform und fasergekoppelten externen Geräten oder anderen photonischen Plattformen zu transferieren. In dieser Arbeit wird ein Aufbau konstruiert, um Fasern so zu modifizieren, dass sie eine adiabatische Modenkopplung in freistehende Wellenleiterstrukturen auf einem Chip ermöglichen. Der Aufbau wurde aus dem Paper von Hauer *et al.* 2014 nachgebaut. Um eine effektive Kopplung zu erreichen, zeigen Simulationen, dass der Durchmesser der Faser im Idealfall auf Submikrometerwerte reduziert werden muss. Dies wird durch eine Heiz- und Zugmethode mit einem Wasserstoffbrenner als Wärmequelle erreicht. Auf diese Weise konnten zuverlässig Fasern im 1μm-Bereich und gelegentlich mit Durchmessern bis zu etwa 300nm erzeugt werden. Im Laufe dieser Arbeit wurde das genutzte Verfahren verbessert und am Ende als Ergebnis vorgestellt.

english version

Quantum computers based on integrated photonic platforms often require a lossless way to transfer photons between the integrated photonic platform and fiber-coupled external devices or other photonic platforms. In this thesis a setup is constructed to modify fibers such that they express adiabatic mode coupling into free standing wave-guide structures on a chip. The setup is recreated from Hauer *et al.* 2014. To achieve effective coupling simulations show that the diameter of the fiber has to be reduced to ideally sub-micrometer values. This is achieved using a heat and pull method with an hydrogen torch as a heat source. Employing this procedure it was possible to reliably create fibers in the 1μm range and occasionally with diameters down to around 300nm. Over the course of creating this thesis the procedure used was optimized and is presented as a result.

Contents

0.1 Motivation and Goal

Quantum based technologies are utilized over a wide range of applications, from the well known Shor's algorithm [2] in cryptography to gravitational measurements in Geo-sciences [3]. One subset of these are Quantum photonics, where operations are done on coherent photons. This can be done in various ways, one of them being photonic integrated circuits (PICs), the optical analog to electronic integrated circuits. More and more applications can be realized on PICs and are increasingly adopted into various fields. Be it computing [4], [5], communications [4], [6]–[8], specialty light sources [9], [10] or detection (e.g. medical imaging)[5], [11], the demands on the efficiency of this technology are increasing [12]. The PICs themselves can now be manufactured in high volume using standard semiconductor manufacturing processes, such as lithography, with ever lower cost and higher efficiency. In contrast coupling guided light, e.g. in an optical fiber, to a PIC is often inefficient[13], [14]. Achieving efficient coupling has proven difficult due to the typically high modal mismatch between fiber ($n_{refractive} \approx 1.5$) and on-chip wave guide (typically $n_{refractive} > 1.8$) regarding spatial extend, polarization and propagation constant. This is caused by the difference in materials used as well as the typical size of a fiber compared to on-chip wave guides. Additionally a region where the light propagates through free-space between fiber and a structure on the chip is often required by the mechanical setup of the coupler. The confined guided modes spatially spread out in free-space, making it hard to confine the light again without losing a significant fraction of power. This poses a problem as low losses are relevant for quantum applications, especially so when working in the single-photon regime, as the lossless collection of all-photons is essential to keep the error rate of such devices low. This problem is addressed by different methods. A popular one is butt coupling on the edge of the PIC chip. The same approach can be used for out-of-plane coupling, where light from the normal direction is coupled into the chip [15], [16]. Coupling can also be realized by mode matching in the strong coupling regime [17], [18].

The different methods all have their advantages and drawbacks: Butt coupling is good for avoiding out-of-plane losses efficiently but proves hard to align, is limited to the edge of a chip and encompasses losses due to scattering. Out-of-plane coupling is already scalable and easy to integrate in the PIC, but relatively high losses compared to adiabatic coupling. Adiabatic coupling, while having near unitary expected coupling efficiency due to adiabatic transition of coupled modes, is not that easily scalable.

The goal of this experiment will be to realize a coupler of the latter kind. As described by Hauer *et al.* 2014 [1] such a coupler can be realized using a heat

and pull method: A Fiber is heated such that a part becomes malleable and pulled such that the malleable part becomes thin to the point where adiabatic coupling into on-chip wave-guides is possible. It is the goal to understand the structure of such a coupler, simulate its behavior and fabricate a fiber which is tapered down and rests upon a tapered diamond wave-guide as seen in figure 1.

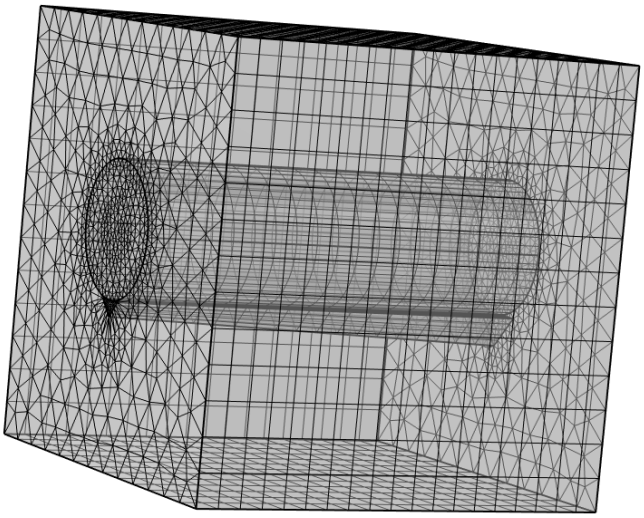

Figure 1: Meshed geometry of a fiber resting upon a tapered wave-guide scaled to fit in a cube. Created using Comsol.

1 Fundamentals

1.1 Physical Description

1.1.1 Maxwell Equations

The Maxwell Equations [19], [20, chapter 4.6] are given here in differential form in SI-units:

$$\begin{aligned} \nabla \cdot \vec{E} &= \frac{\rho}{\varepsilon_0} \quad \text{(a)} & \nabla \cdot \vec{B} &= 0 \quad \text{(b)} \\ \nabla \times \vec{E} &= -\frac{\partial \vec{B}}{\partial t} \quad \text{(c)} & \nabla \times \vec{B} &= \mu_0 \left(\vec{J} + \varepsilon_0 \frac{\partial \vec{E}}{\partial t} \right) \quad \text{(d)} \end{aligned} \tag{1.1}$$

$\vec{E}$ - electric field; $\vec{B}$ - magnetic field; $\vec{J}$ - current density; ρ - charge density; ε_0 - vacuum permitivity; μ_0 - vacuum permeability

Any optical scenario can be described in terms of Maxwell's Equations, they are a complete classical description. Typically they are solved for the electric and magnetic fields, but only in simple cases an analytical solution can be found. In more complex cases the solution can be approximated numerically.
As for any differential equation to get a unique solution it is necessary to know the boundary and initial conditions. For example, with no charges and no currents anywhere the equations can be separated [20, chapter 7.1]. This is done by taking the curl of equation 1.1 c (d), applying the identity $\nabla \times (\nabla \times \vec{A}) = \nabla(\nabla \cdot \vec{A}) - \nabla^2 \vec{A}$ for a vector field $\vec{A}$ and inserting 1.1 a (b) into it. This yields

$$\mu\varepsilon \frac{\partial^2 \vec{E}}{\partial t^2} - \nabla^2 \vec{E} = 0, \qquad \mu\varepsilon \frac{\partial^2 \vec{B}}{\partial t^2} - \nabla^2 \vec{B} = 0. \tag{1.2}$$

These are well known differential equations, the so called Helmholtz Equations. Solutions to these sorts of problems, besides the trivial solution $E = 0 = B$, are wave equations:

$$\vec{E}(\vec{r}) = E_0 e^{-i(\vec{k}\vec{r} - \omega t)}, \quad \vec{B}(\vec{r}) = B_0 e^{-i(\vec{k}\vec{r} - \omega t)}, \tag{1.3}$$

where $\vec{r}$ is a position vector. This equation represents a linearly polarized pla-

nar wave traveling in direction $\vec{k}$. Because the divergence of the electric and magnetic fields are zero, the wave is transverse, meaning there are no fields in the direction of propagation. The phase velocity is given by

$$v_p = \frac{\omega}{k} = \frac{1}{\sqrt{\mu_0 \mu_r \varepsilon_0 \varepsilon_r}}. \tag{1.4}$$

1.1.2 Wave-Guide

A wave that can freely expand into all three dimensions loses in intensity according to the inverse square law. A wave-guide is a structure which limits the propagation to one dimension and thereby conserves most of its energy.
Let us consider a wave-guide in which a wave travels. To simplify we will focus only on two dimensions and look at only one interface of the wave-guide. The interface is the border between the wave-guide material with refractive index n_1 and its cladding with refractive index n_2. A beam traveling in the wave-guide and incident to the interface under an angle (measured to the normal of the interface) θ_1 is refracted to travel inside the cladding under an angle θ_2 [20, chapter 8.4.2]. This is given by Snell's law

$$n_1 \sin(\theta_1) = n_2 \sin(\theta_2). \tag{1.5}$$

It follows that there might be a critical incident angle θ_c under which the outgoing beam would be parallel to the interface ($\theta_2 = 90°$). This is given by

$$\theta_c = \arcsin\left(\frac{n_2}{n_1}\right). \tag{1.6}$$

Angles greater than this critical angle can not leave the wave-guide. This phenomenon is also referred to as total internal reflection.

We will continue with such a perfectly reflecting interface parallel to the x-axis [20, chapter 7.9.1]. Since any wave traveling in any direction can be decomposed into infinite plane waves it is enough to look at an arbitrary plane wave with an angle of incidence θ. This wave can be split into one component parallel and one normal to the interface:

$$\vec{E}_{incident} = \hat{y} E_0 \exp\left(i\omega t - \vec{k}\vec{r}\right) = \hat{y} E_0 \exp\left(i\omega t - k_x x - k_z z\right). \tag{1.7}$$

The reflected wave differs from the incident one only by a flipped sign of the propagation constant k_z normal to the interface. Superposition of those two

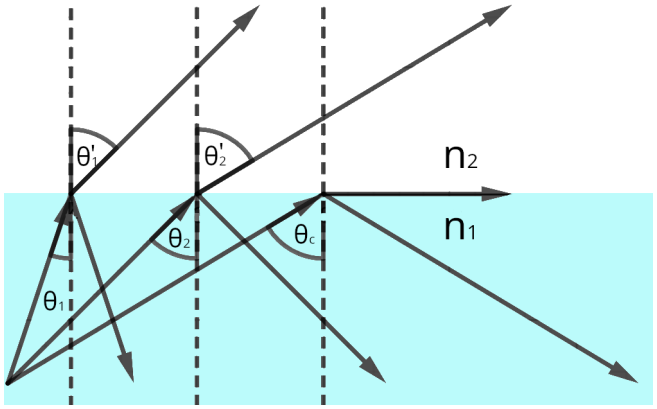

Figure 1.1: Incoming light beam getting reflected at a boundary between two materials with different refractive index. Created using oPhysics[21].

waves yields

$$\vec{E}_{tot} = \hat{y}E_0 \exp\left(i\omega t - k_x x - k_z z\right) + \hat{y}E_0 \exp\left(i\omega t - k_x x + k_z z\right) \tag{1.8}$$

$$= \hat{y}E_0 \exp\left(i\omega t - k_x x\right)\left(\exp\left(-ik_z z\right) + \exp\left(ik_z z\right)\right) \tag{1.9}$$

using $\cos(x) = 1/2(e^{-ix} + e^{ix})$ and taking the real part to get a physical result

$$\vec{E}_{tot} = 2\hat{y}E_0 \cos\left(\omega t - k_x x\right)\cos\left(k_z z\right). \tag{1.10}$$

We identify the first cosine to be a traveling wave which propagates (in x) through the wave-guide and the second cosine to be a standing wave (in z) referred to as the transverse electric mode or TE-mode. An analogous equation can be derived when using the magnetic field $\vec{H}$. Here, the second cosine would be referred to as the transverse magnetic mode or TM-mode.

1.1.3 Strong Coupling

The interaction between quantum systems is typically studied in the weak and strong coupling limits. In the strong coupling regime the interaction energy is so large that back transfer to the donor becomes possible and thus it is no longer possible to distinguish between donor and acceptor. This necessitates the pair to be described as one system, which can also be understood as a delocalization of the excitation. Energy level splitting is another characteristic feature of the strong coupling regime and will be discussed in the classical as well as in the quantum mechanical framework.[22]

Classical View

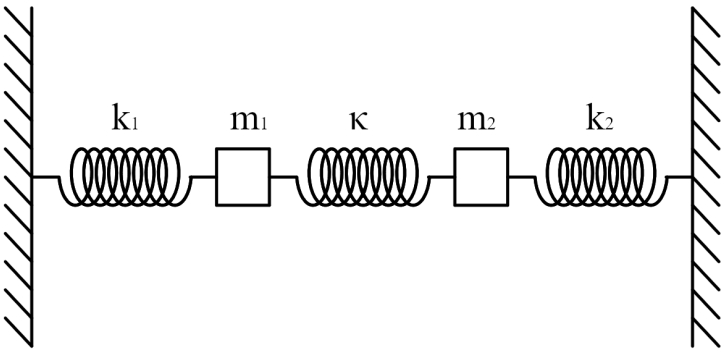

Figure 1.2: Two coupled oscillators, consisting of two masses m_i on springs k_i which are coupled by a third spring κ. Created using oPhysics[21].

Suppose two coupled oscillators (figure 1.2) with eigenfrequencies $\omega_{\mathrm{I}}^0 = \sqrt{k_{\mathrm{I}}/m_{\mathrm{I}}}$, $\omega_{\mathrm{II}}^0 = \sqrt{k_{\mathrm{I}}/m_{\mathrm{I}}}$ and coupling constant κ [22][23, chapter 11.8]. Their equation of motion without dissipation of energy

$$m_i\ddot{x}_i + k_i x_i + \kappa(x_i - x_j) = 0 \tag{1.11}$$

with the Ansatz

$$x_i(t) = x_i^0 \exp\left(-i\omega_{\pm}t\right) \tag{1.12}$$

yield, besides the trivial solution, the new eigenfrequencies $\omega_{\pm}$. Because the system is (strongly) coupled it does not make sense to attribute the frequencies to one of the oscillators; we have to view both oscillators as one system:

$$(\omega_{\pm})^2 x_i(t) + \underbrace{\frac{k_i + \kappa}{m_i}}_{:=\omega_i^2} x_i(t) - \frac{\kappa}{m_i} x_j(t) = 0. \tag{1.13}$$

The two resulting linear equations can be written as a Matrix $\mathbf{M}$

$$\mathbf{M} \cdot \vec{x} = \begin{pmatrix} \omega_{\pm}^2 + \omega_{\mathrm{I}}^2 & -\frac{\kappa}{m_{\mathrm{I}}} \\ -\frac{\kappa}{m_{\mathrm{II}}} & \omega_{\pm}^2 + \omega_{\mathrm{II}} \end{pmatrix} \cdot \begin{pmatrix} x_{\mathrm{I}}(t) \\ x_{\mathrm{II}}(t) \end{pmatrix} = 0. \tag{1.14}$$

Non trivial solutions only exist if the determinant of $\mathbf{M}$ vanishes.

$$\det(\mathbf{M}) = (\omega_{\pm}^2 + \omega_{\mathrm{I}}^2) \cdot (\omega_{\pm}^2 + \omega_{\mathrm{II}}^2) - \frac{\kappa^2}{m_{\mathrm{I}} m_{\mathrm{II}}} \tag{1.15}$$

$$= \omega_{\pm}^4 + \omega_{\pm}^2(\omega_{\mathrm{I}}^2 + \omega_{\mathrm{II}}^2) + \omega_{\mathrm{I}}^2\omega_{\mathrm{II}}^2 - \frac{\kappa^2}{m_{\mathrm{I}} m_{\mathrm{II}}} \stackrel{!}{=} 0. \tag{1.16}$$

This is a quadratic equation for $\omega_\pm^2$ and is solved by

$$\omega_\pm^2 = \frac{\omega_\mathrm{I}^2 + \omega_\mathrm{II}^2}{2} \pm \sqrt{\frac{(\omega_\mathrm{I}^2 + \omega_\mathrm{II}^2)^2}{4} - (\omega_\mathrm{I}^2\omega_\mathrm{II}^2 - \frac{\kappa^2}{m_\mathrm{I} m_\mathrm{II}})} \tag{1.17}$$

$$= \frac{1}{2}\left(\omega_\mathrm{I}^2 + \omega_\mathrm{II}^2 \pm \sqrt{\omega_\mathrm{I}^4 + 2\omega_\mathrm{I}^2\omega_\mathrm{II}^2 + \omega_\mathrm{II}^4 - 4\omega_\mathrm{I}^2\omega_\mathrm{II}^2 + 4\frac{\kappa^2}{m_\mathrm{I} m_\mathrm{II}}}\right) \tag{1.18}$$

$$= \frac{1}{2}\left(\omega_\mathrm{I}^2 + \omega_\mathrm{II}^2 \pm \sqrt{(\omega_\mathrm{I}^2 - \omega_\mathrm{II}^2)^2 + 4\frac{\kappa^2}{m_\mathrm{I} m_\mathrm{II}}}\right). \tag{1.19}$$

The energy splitting at the crossing point ($\omega_\mathrm{I} = \omega_\mathrm{II}$) is proportional to the splitting of the square angular frequencies and given by

$$\Gamma := \omega_+^2 - \omega_-^2 = \sqrt{\underbrace{\left(\omega_\mathrm{I}^2 - \omega_\mathrm{II}^2\right)^2}_{=0} + 4\frac{\kappa^2}{m_\mathrm{I} m_\mathrm{II}}}. \tag{1.20}$$

Noticeably, the splitting is proportional to the coupling constant $\lambda_0 \propto \kappa$. The anticrossing resulting from the energy split is therefore a characteristic trait for strong coupling. Although our analysis was purely classical, a quantum mechanical analysis yields an analog energy splitting, as will be shown in the next section.

Quantum Mechanical View

We want to consider a Hamiltonian consisting of two field modes and their interaction:

$$\hat{H} = \hat{H}_{field\mathrm{I}} + \hat{H}_{field\mathrm{II}} + \hat{H}_{interact} \tag{1.21}$$

First we take a look at the hamiltonian of the quantized electric field [24, page 99] which can be reduced to only the modes of interest under the assumption that all other modes are sufficiently detuned:

$$\hat{H}_{field} = \sum_{k,\lambda} \hbar\omega_k \left(a_{k,\lambda}^\dagger \hat{a}_{k,\lambda} + \frac{1}{2}\right) \quad \overset{\text{reduce}}{\rightarrow} \quad \hbar\omega_\mathrm{I}\left(a_\mathrm{I}^\dagger \hat{a}_\mathrm{I} + \frac{1}{2}\right) + \hbar\omega_\mathrm{II}\left(a_\mathrm{II}^\dagger \hat{a}_\mathrm{II} + \frac{1}{2}\right), \tag{1.22}$$

where $\hat{a}^\dagger$ is the creation, $\hat{a}$ the annihilation operator and ω_k the frequency of the mode. To describe the interaction between the two modes of interest a

interaction Hamiltonian is formulated:

$$\hat{H}_{interact} = \sum_{k,\lambda} \hat{E}_{k,\lambda} \cdot \left(\sum_{\substack{k' \neq k \\ \lambda' \neq \lambda}} \hat{E}_{k',\lambda'} \right) \quad \overset{\text{reduce}}{\rightarrow} \quad \hat{E}_{\mathrm{I}} \hat{E}_{\mathrm{II}} + \hat{E}_{\mathrm{II}} \hat{E}_{\mathrm{I}}. \tag{1.23}$$

With $u_{k,\lambda}$ representing the envelope functions and normalization N the Electric field operator of one discrete mode [24, page 96] is given by

$$\hat{E}(R)_{k,\lambda} = N_k u_{k,\lambda} \left(\hat{a}_{k,\lambda} e^{ik \cdot R} - \hat{a}^{\dagger}_{k,\lambda} e^{-ik \cdot R} \right). \tag{1.24}$$

Defining Location dependent factors $b = N_k u_{k,\lambda} e^{ik \cdot R}$ for each of the modes, the reduced interaction can be written as

$$\hat{H}_{interact} = \left(b_{\mathrm{I}}(R_{\mathrm{I}}) \hat{a}_{\mathrm{I}} - b^*_{\mathrm{I}}(R_{\mathrm{I}}) \hat{a}^{\dagger}_{\mathrm{I}} \right) \cdot \left(b_{\mathrm{II}}(R_{\mathrm{II}}) \hat{a}_{\mathrm{II}} - b^*_{\mathrm{II}}(R_{\mathrm{II}}) \hat{a}^{\dagger}_{\mathrm{II}} \right) \tag{1.25}$$

Multiplication yields these four interaction terms:

- $\hat{a}^{\dagger}_{\mathrm{I}} \hat{a}_{\mathrm{II}}$ create field excitation one, annihilate field excitation two
- $\hat{a}_{\mathrm{I}} \hat{a}^{\dagger}_{\mathrm{II}}$ annihilate field excitation one, create field excitation two
- $\hat{a}_{\mathrm{I}} \hat{a}_{\mathrm{II}}$ annihilate both field excitation
- $\hat{a}^{\dagger}_{\mathrm{I}} \hat{a}^{\dagger}_{\mathrm{II}}$ create both field excitation

While the first two terms conserve energy when perfectly in resonance ($\omega_{\mathrm{I}} - \omega_{\mathrm{II}} = 0$) the latter two represent a loss or gain of $\hbar(\omega_{\mathrm{I}} + \omega_{\mathrm{II}})$. Neglecting those not energy conserving terms[1] and inserting everything in our initial equation we arrive at

$$\hat{H} = \hbar\omega_{\mathrm{I}} \left(a^{\dagger}_{\mathrm{I}} \hat{a}_{\mathrm{I}} + \frac{1}{2} \right) + \hbar\omega_{\mathrm{II}} \left(a^{\dagger}_{\mathrm{II}} \hat{a}_{\mathrm{II}} + \frac{1}{2} \right) - \hbar \left(b^*_{\mathrm{I}} b_{\mathrm{II}} \hat{a}^{\dagger}_{\mathrm{I}} \hat{a}_{\mathrm{II}} + b_{\mathrm{I}} b^*_{\mathrm{II}} \hat{a}_{\mathrm{I}} \hat{a}^{\dagger}_{\mathrm{II}} \right) \tag{1.26}$$

which is very similar to the Jaynes-Cummings Hamiltonian for Atom-field interactions:

$$\hat{H}_{JC} = \hbar\omega_c \left(\hat{a}^{\dagger}_c \hat{a}_c + \frac{1}{2} \right) + \hbar\omega_{eg} \left| e \right\rangle \left\langle e \right| + \hbar g_c \left(\hat{\sigma}_+ \hat{a}_c + \hat{\sigma}_- \hat{a}^{\dagger}_c \right) \tag{1.27}$$

[1] in the Jaynes-Cummings Hamiltonian these terms would be callled "counter rotating" and neglecting those is called the Rotating wave approximation (RWA)

In the basis $(|m+1,n\rangle, |m,n+1\rangle)^T$ and neglecting the constant offsets $\frac{1}{2}\hbar\omega_{\mathrm{I}}$ and $\frac{1}{2}\hbar\omega_{\mathrm{II}}$ the Hamiltonian takes the form of

$$\hat{H}_{m,n} = \begin{pmatrix} \langle m+1,n|\,\hat{H}\,|m+1,n\rangle & \langle m+1,n|\,\hat{H}\,|m,n+1\rangle \\ \langle m,n+1|\,\hat{H}\,|m+1,n\rangle & \langle m,n+1|\,\hat{H}\,|m,n+1\rangle \end{pmatrix} \tag{1.28}$$

$$= \hbar \begin{pmatrix} \omega_{\mathrm{I}}(m+1)+\omega_{\mathrm{II}}n & b_{\mathrm{I}}^* b_{\mathrm{II}}\sqrt{m+1}\sqrt{n+1} \\ b_{\mathrm{I}} b_{\mathrm{II}}^*\sqrt{m+1}\sqrt{n+1} & \omega_{\mathrm{I}}m+\omega_{\mathrm{II}}(n+1) \end{pmatrix} \tag{1.29}$$

for the simple ground state case $m=0$, $n=0$ the Hamiltonian looks much simpler:

$$\hat{H}_{0,0} = \hbar \begin{pmatrix} \omega_{\mathrm{I}} & b_{\mathrm{I}}^* b_{\mathrm{II}} \\ b_{\mathrm{I}} b_{\mathrm{II}}^* & \omega_{\mathrm{II}} \end{pmatrix} \tag{1.30}$$

The calculation with $m,n \in \mathbb{N}$ is not much harder but the result is much more convoluted. The simpler case is enough to motivate a quantum mechanical strong coupling between electromagnetic field modes. Diagonalization or setting $\det(\mathbf{H}-\lambda\mathbf{I})=0$ yields eigenvalues

$$E_{\pm} = \hbar\left(\frac{\omega_{\mathrm{I}}+\omega_{\mathrm{II}}}{2} \pm \sqrt{\left(\frac{\omega_{\mathrm{I}}-\omega_{\mathrm{II}}}{2}\right)^2 + |b_{\mathrm{I}}|^2|b_{\mathrm{II}}|^2}\right). \tag{1.31}$$

Again calculating the energy splitting at the crossing point yields a result remarkably similar to the one from the classical view:

$$\Gamma := E_+ - E_- = 2\hbar\sqrt{\underbrace{\left(\frac{\omega_{\mathrm{I}}-\omega_{\mathrm{II}}}{2}\right)^2}_{=0} + |b_{\mathrm{I}}|^2|b_{\mathrm{II}}|^2}. \tag{1.32}$$

The product of the norms of b_{I} and b_{II} can therefore be understood as a coupling constant. This constant is dependent on the product of both envelope functions meaning the more 'overlap' those two envelopes have the stronger the coupling.

1.1.4 Adiabatic Mode Conversion

The results from the last section for both cases, the classical and the quantum mechanical one, were two coupled modes, which form new modes. They exhibit an energy splitting proportional to the coupling constant.
In both cases the system follows the same Eigenstate if tuned at the right speed through the resonance and therefore transfers energy, either from one oscillator to the other or from one field mode to the other and vice versa. This is called an adiabatic transition. [22]
If the tuning happens too fast, the coupling has not enough time to interact

and the transition becomes diabatic, crossing the energy gap. This can also be understood in terms of the uncertainty between time and energy.

1.1.5 Physics of Mechanical Setup and Flame

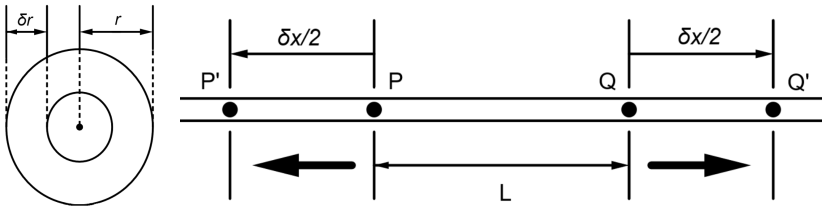

Figure 1.3: A fiber of radius r and over a length of the hotzone L is stretched in a time interval δt from point P and Q to P' and Q' elongating by δx and shrinking by δr. Created using oPhysics[21].

The following part follows closely a paper from Birks (1992) [25]. We consider an initial region of fiber between point P and Q with length L_0 and radius r_0 at time $t = 0$. We now distinguish between fiber length $x := L_f$ and hot-zone length L_h in which the fiber is hot and deformable, and everywhere else cold and rigid. In each time step δt P and Q move with a velocity v to Points P' and Q'. This means from $t \to t + \delta t$ follows $r \to r + \delta r$, $x \to x + \delta x$ and $L_h \to L_h + \delta L_h$. We assume that the mass and therefore volume of the fiber must be conserved, resulting in

$$\pi r^2 L_f = \pi(r + \delta r)^2 (L_f + \delta x) = \pi r^2 L_f + 2\pi r L \delta r + \pi r^2 \delta x + O(2). \tag{1.33}$$

In the limit $\delta t \to 0$ we can discard terms of higher order O(2) and can rearrange to get the differential equation

$$\frac{\partial r}{\partial x} = \frac{-r}{2L}. \tag{1.34}$$

If the taper forms symmetrically then the taper length z is connected to the elongation x by

$$2z = x + L_h(t = 0) - L_h(t). \tag{1.35}$$

Everything until now works even with non constant hot-zone ($\delta L_h \neq 0$). We will now fix the hot-zone[2] at a constant $L_h(t) = L_h(t = 0)$. This makes the following easier: we integrate 1.34 by separating the variables with initial condition $r(t = 0) = r_0$ and replace via 1.35 x with $2z$ which yields

$$r(z) = r_0 \exp\left(-\frac{z}{L}\right). \tag{1.36}$$

[2]for the general solution consult Birks1992 [25]

Remarkably, the result does neither depend on the time pulled nor on the velocity with which the fiber was stretched but only on the size of the hot-zone and the length it was stretched. To avoid confusion: For constant pull velocity a longer pull time still results in a greater length over which the fiber was stretched and therefore the smallest radius is smaller than for shorter pull times.
One obvious limiting factor of this model is the assumption that the hot-zone is well defined in its length as the fiber is typically heated by a flame which heats different parts of the fiber to different temperatures, resulting in a gradual transition out of the hot-zone.
A different method exists to achieve a better approximation to a constant hot zone which is sometimes referred to as the "flame brush" method. A thin ideally point like torch is moved along the desired hot-zone length back and forth with constant speed. If the speed of the flame is fast compared to the speed of the taper elongation, the fiber should be approximately identically heated, because the surrounding air is a good insulator.
For this experiment the only way to change the size of the hot zone is to switch between different orifice sizes for the hydrogen torch and adjusting the height of the flame.

1.2 Simulation

Two types of simulations were performed in this thesis. The goal of the first one was to verify that we are indeed in the strong coupling regime and the goal of the second one to check which combination of parameters leads to the most efficient coupling from fiber to wave-guide.
This section will explain how the two used simulation methods (FEM/FDTD) work, which assumptions went into the simulation and briefly cover the obtained results. The points discussed under general remarks apply to both simulations while the two sections afterwards only apply to the respective simulation.

1.2.1 General Remarks

Discrete Maxwell Equations

To use the Maxwell Equations in numerical simulations they have to be discretized [26]. This reduces the problem from an infinite-dimensional problem with respect to the values of the E- and B-field to a finite set of solvable equations. The methods used here are mesh based, in practice a mesh might not follow cartesian coordinates and even change in orientation and scaling for different parts of the simulation. This complex mesh and the subsequent approximation of the equations is done by specialized programs. The principle by which the

approximations are derived for the different methods is fundamentally different, but to show the basic idea behind a discrete representation, the first component of equation 1.1 c in Cartesian coordinates is given as an example. The following notation is used for grid points and functions of space and time in a grid with side lengths Δx, Δy, Δz and time intervals Δt:

$$(i,j,k) := (i\Delta x, j\Delta y, k\Delta k) \qquad F^n(i,j,k) := F(i\Delta x, j\Delta y, k\Delta k, n\Delta t) \tag{1.37}$$

$$\frac{\partial E_y}{\partial z} - \frac{\partial E_z}{\partial y} = \frac{\partial B_x}{\partial t} \tag{1.38}$$

$$\Rightarrow \frac{E_y^n(i,j,k-\frac{1}{2}) - E_y^n(i,j,k+\frac{1}{2})}{\Delta z} - \frac{E_z^n(i,j-\frac{1}{2},k) - E_z^n(i,j+\frac{1}{2},k)}{\Delta y} \tag{1.39}$$

$$= \frac{B_x^{n+\frac{1}{2}}(i,j,k) - B_x^{n-\frac{1}{2}}(i,j,k)}{\Delta t} \tag{1.40}$$

Geometry

The geometry described here is used for both simulations. Slight variations will be discussed separately. We will assume that the wave-guide structure is free-standing and its distance from the substrate is so large that the wave-guide mode is not influenced by the substrate's refractive properties. In figure 1.2.1 a cross section of the geometry can be seen. The fiber is represented by a circle with radius r. The wave-guide is a triangular structure with width w and two angles on this edge with 45°. This is because the wave-guides are expected to be released from bulk diamond via Faraday cage angled etching [27]. They are enclosed by a rectangular domain of air chosen to be large enough such that no meaningful part of the solution gets in contact with the scattering boundary condition at the outer edge of the domain. The different domains have different refractive indices given in table 1.1.

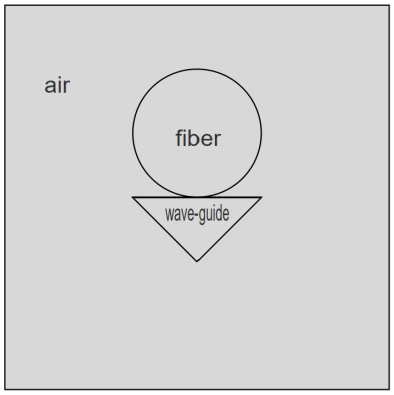

Figure 1.4: cross section of geometrical setup in the simulation

Table 1.1: refractive indices for the domains of the simulation at the wavelength of 1550 nm

name	refractive index
air	1
diamond	2.4
glass fiber	1.5

1.2.2 Finite Element Method (FEM) in Comsol

Finite Element Method (FEM)

Finite Element Method [28, chapter 6.3.2] is a numerical method to solve boundary value problems. A mesh is used to subdivide a complex geometry into smaller simpler parts, the name-giving finite elements. This is achieved by discretization, with each sub-domain governed by the equations of the underlying problem. The solutions of these subsections are then assembled again to form the solution of the initial problem.

Simulation Assumptions

This simulation is done in COMSOL Multiphysics® [29]. A two dimensional crosssection of the geometry described in section 1.2.1 is simulated for different values of the fiber radius r and the wave-guide width. For each step the mode was chosen for which the effective refractive index is closest to the step before.

Simulation Results

Per radius and width there were three simulations calculated. The modes of the fiber, the mode of the wave-guide and the combined mode. The results were plotted in figure 1.5d and show a clear energy splitting, which indicates that we are indeed in the strong coupling regime, as discussed in section 1.1.3.

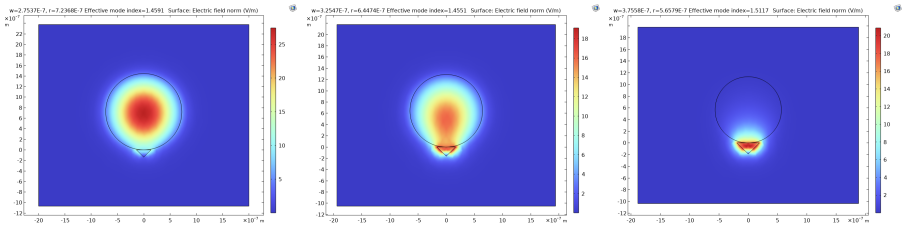

(a) quasi fiber mode (b) combined mode (c) quasi wave-guide mode

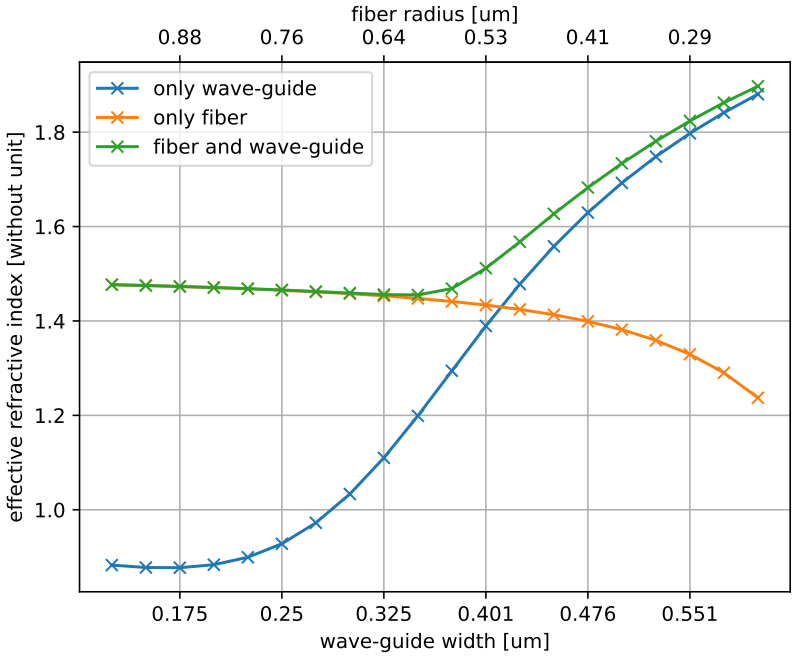

(d) Diagram along the taper regions. Both the radius and the waveguide width were tapered simultaneously

Figure 1.5: FEM Simulation results. (a) to (c) show the intensity distribution of some of the simulated modes and (d) shows the effective refractive index at every simulation point.

1.2.3 Finite Difference Time Domain (FDTD) in Lumerical

To understand the FDTD method more easily we will first discuss the simpler leapfrog scheme.

Leapfrog Scheme

The leapfrog scheme [28, page 396] or leapfrog integration is a tool in numerical analysis to integrate second order differential equations of the form

$$\frac{d^2x}{dt^2} = A(x) \quad \text{or equivalently} \quad \frac{dx}{dt} = v; \frac{dv}{dt} = A(x). \tag{1.41}$$

The equations to update the variable x and its rate of change over time v are given by

$$v_{i+1/2} = v_{i-1/2} + A(x_i) \cdot \Delta t \tag{1.42}$$

$$x_{i+1} = x_i + v_{i+1/2} \cdot \Delta t \tag{1.43}$$

and to get v_i one can simply calculate

$$v_i = v_{i-1/2} + A(x_i) \cdot \Delta t/2 \tag{1.44}$$

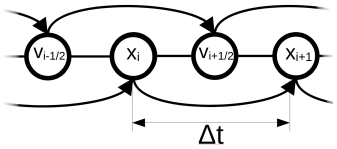

Figure 1.6: ilustration of the leapfrog scheme

Finite-Difference-Time-Domain Method (FDTD)

The Finite-Difference Time-Domain method or Yee's method is used to solve Maxwells equations numerically[26]. Examining these equations one finds, that the change of the magnetic field in time is dependent on the spatial distribution of the E-field, to be more precise its curl. The E-field is, analogously, dependent on the curl of the B-field and the electric current density, the latter we will disregard for now.
In one dimension this looks very much like the leapfrog scheme which we discussed beforehand. Instead of place and velocity the electric and magnetic field are offset from each other. For a given starting condition the time evolution of this 1 dimensional domain can be computed. This of course gets more complicated in 3 dimensions as we have to compute the curl in 3 dimensions. This can be visualized in different ways. For example in 1.7 we see that the quantities are computed for every edge of a box and therefore in the center of the face of the box the other quantity can be computed. This staggering is also referred to as Yee's lattice. From this the TE and TM modes can be easily extracted by just looking on one of the faces of the cube and taking all the values perpendicular to the normal of the face.

Simulation Assumptions

The simulation discussed in the following was performed using Ansys Lumerical FDTD[30]. The geometry described in section 1.2.1 is simulated in three dimensions. This can be divided into three sections. The starting section with a length of 10μm consists of the fiber with diameter d and the wave-guide with

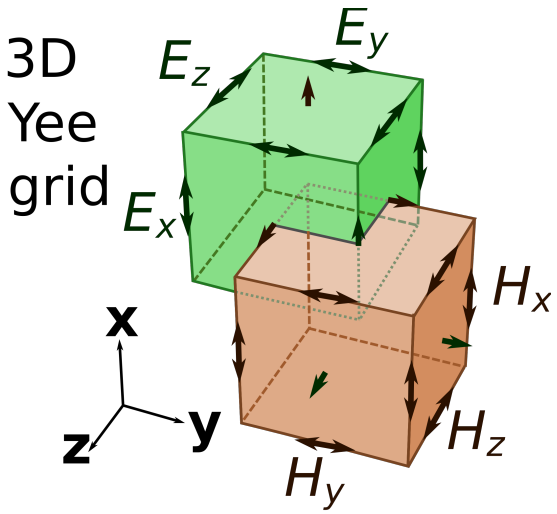

Figure 1.7: Yees's lattice. Modified from FDominec, CC BY-SA 4.0, via Wikimedia Commons

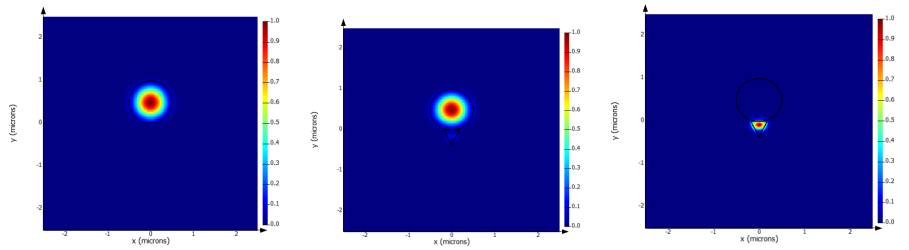

Figure 1.8: Modes used in the FDTD simulation. From left to right: fiber mode (used as exitation), fundamentel fiber mode and fundamental wave-guide mode

width w. The center section is defined by the variable taper length, over which the waveguide is linearly tapered down to a width of 10 nm. The end section consists of just a 10μm long fiber. The fiber diameter is constant within the simulation domain. On both ends of the simulation domain a port is created. The excitation signal is a mode source at the end port. This mode is chosen to be TE-like (horizontal electric field distribution). The S-parameters for transmission into the fundamental modes of the wave-guide and the fiber at the start port are calculated. The modes can be seen in figure 1.8

Simulation Results

As the accuracy of the auto non-uniform mesh in lumerical can be chosen on an integer scale from 1 (coarse mesh) to 8 (fine mesh) the impact of this setting was examined. To that end the same geometry for different mesh-accuracies was simulated. The results do not show a clear point of stabilization at higher

mesh-accuracy. For a broader overview a larger sweep with mesh-accuracy 3 was done and a smaller sweep with mesh-accuracy 7 for comparison was performed. The coupling efficiency for different fiber diameters and taper lengths are shown in figure 1.9. Although the simulations do not agree on a numerical level, in both simulations two major trends become visible. With smaller diameter more energy is transmitted into the wave-guide mode. Similarly with longer taper length the coupling efficiency increases. From what was discussed in the theory (section 1.1.4) one would expect to see back transfer of energy if the taper length becomes sufficiently large, but this seems not yet to be the case.
In conclusion the fabrication of the tapered-fiber should focus on achieving small diameters and appropriate bending such that structures on the chip can be targeted precisely. The interaction length can then be adjusted on the chip, lengths over or equal to 40μm seem ideal a upper limit is dictated by the mentioned back transfer but not investigated here.

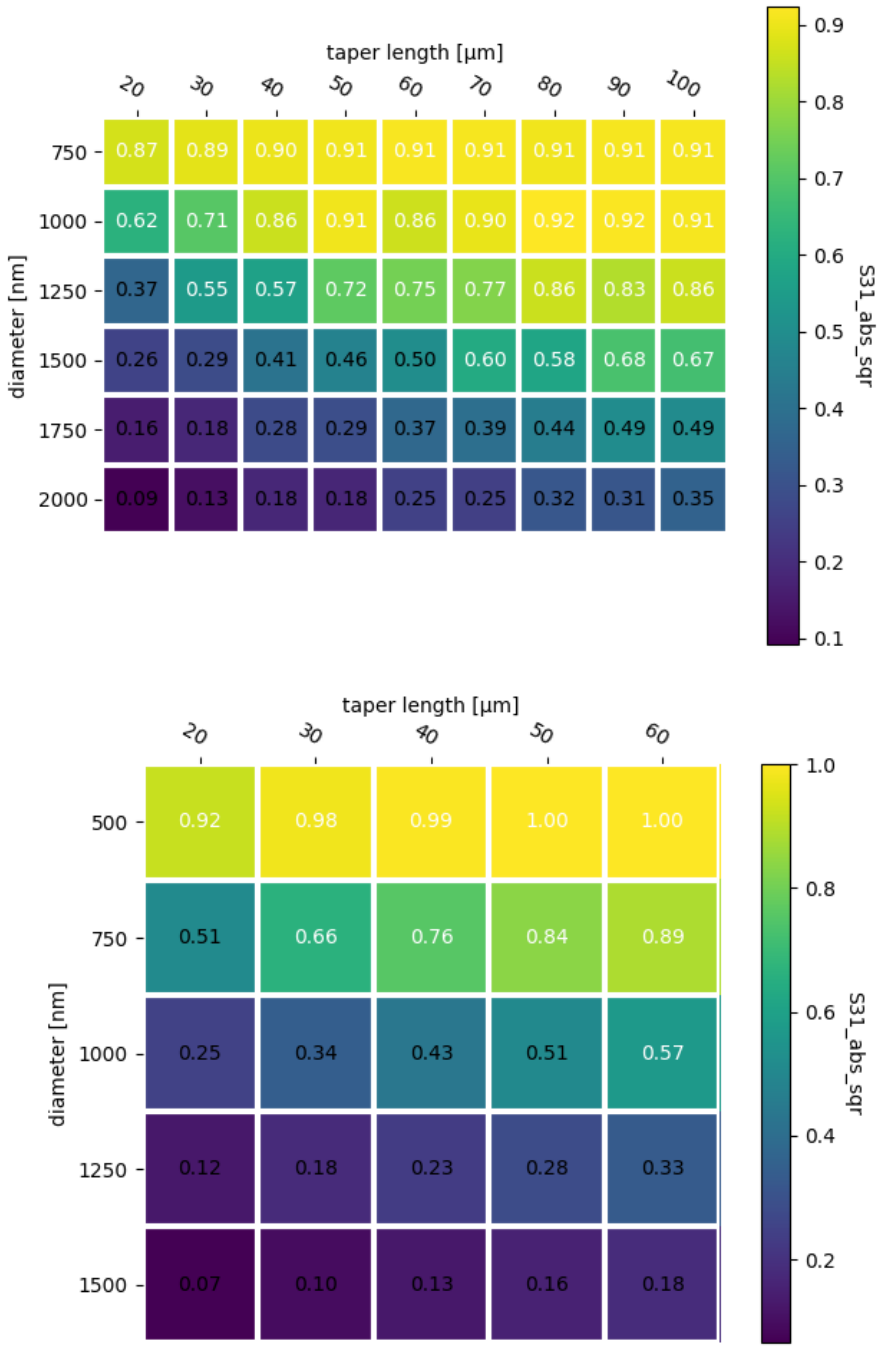

Figure 1.9: FDTD results. Plotted are the S-parameters associated with the coupling from the exited fiber mode to the wave-guide mode. Above the larger sweep using mesh accuracy 3; below the smaller sweep using mesh accuracy 7

2 | Experiment

2.1 Fiber Tapering Setup

The setup can be separated in 5 parts: The hydrogen torch, the fiber pull contraption, a stage system for gluing, a microscope and a transmission tracking mechanism. These are discussed below, although minor components like adapter-plates[1], or screws, etc. will not be discussed. Beyond that a fiber fusion splicer (FITEL S179A 3-axis splicer) and a fiber cleaver are used to prepare fibers with connector ports on both ends.

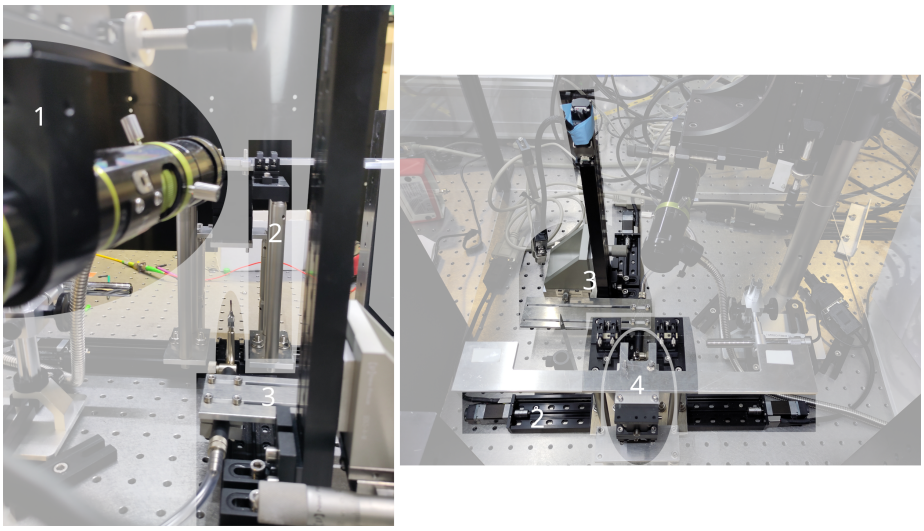

Figure 2.1: Parts of the Setup: 1) Microscope 2) fiber pull contraption 3) hydrogen torch 4) stage system for gluing

The Hydrogen Torch is mounted on a z-stage (Zaber LSM200A-E03T4A) to adjust its height with respect to the fiber via an angle bracket (Newport 9063-A-M). This is mounted to a second linear stages (Zaber LSM200A-E03T4A) for moving the flame under the fiber or away from it. Between both stages a third manual linear stage (Newport 9063-COM-M Gothic-Arch 65mm Platform Translation stage) allows the flame to be adjusted along the fiber. The tip of the torch can be changed to create a wider or narrower flame, adjusting the hot-zone length.
As a variation another hydrogen torch can be connected to the same hydrogen line such that both flames face each other (one down; one up)

[1] most of the manufactured adapter plates can be found in the appendix 5

The Fiber Pull Contraption consist out of a bare fiber holder (Newport 466A-710), on top of two optical posts which are mounted on a linear stage (y-direction) moving perpendicular to the linear stage of the hydrogen torch. The same is mirrored at the flame position such that the second linear stage, with its fiber holder, moves in negative y-direction. The optical posts are needed to make enough room for the various heights at which the hydrogen torch can be.

The Stage System for Gluing consists out of a manual xyz-stage (Newport M-DS40-XYZ) which has a aluminum plate on top with 2 screws to mount support structures for the fiber. These were either silicon chips for measuring their diameter via SEM or a U-shaped holder (aluminum fork) designed to keep the tapered part of the fiber floating in mid air, designed to be implemented in an adiabatic measurement scheme. To glue the fiber to these structures double sided tape or an epoxy glue was used.

The Microscope is mounted at an slight angle but almost parallel to the torch stage (x-direction). This allows the experimenter to examine the shape of the fiber taper in real time during the pulling process.

The Transmission Tracking Mechanism consists of a fiber-ended laser connected to the fiber to be pulled. On the other port of the fiber a photo-diode is connected whose electrical signal is read out and displayed on a monitor. This allows for a real time monitoring of the transmission of the taper.

2.2 Methods

This section will cover the methods used during the experiment, which were developed or tested within the scope of this thesis. This includes the testing of methods, which did not provide an expected result in the end. In that regard, this section will already discuss the fruitfulness of some approaches before the results section.
The final most promising procedure will be described in section 3.1 results and outlook.

2.2.1 Fiber Preparation

Three methods of removing the outer layers have been tested. The fibers used had 4 layers which needed to be removed: An outer jacket, buffering fibers, a buffer jacket and a coating on top of the cladding.
The first layer was easily removed mechanically. Especially when working on

a fiber end a fiber stripper can be used. But using a knife to make two cuts around the fiber and one connecting the two cuts, made it possible to simply remove a section in the middle of a fiber as well. The buffering strings are cut with scissors. The buffer jacket and coating were tried to be removed using the hydrogen torch, acid or mechanical means with varying degrees of success.

Using the Hydrogen Flame to burn away the coatings is quite effective but does easily melt the fiber as well. In the most extreme case this leads to deformation of the fiber, or in less extreme cases it meant that while the coating is turned to presumably mostly carbon it also bound to the fiber. A less aggressive, less hot flame might be enough to burn away the coating without melting the fiber.

Using Acid in particular sulfuric acid did not seem to affect the coatings much. Boiling and constantly stirring the sulfuric acid might bring an improvement but this would need increased security measures.

Mechanically removing the remaining two coatings only worked well when using a fiber stripper designed to do exactly that. This had the disadvantage of requiring a fiber end without a connector. If one wanted connectors on both ends of the fiber the most effective strategy was to fusion splice one onto the fiber after removing the coatings.

2.2.2 Heat and Pull

First a fiber is secured in the fiber holders. The hydrogen torch moves until positioned under the fiber. At this point a timer starts and the two stages on which the fiber holders are mounted start to pull with velocity v. The timer terminates at time t either when the specified time has elapsed or when the experimenter notices that the fiber is close to breaking and stops the procedure. In both cases the stages stop pulling and the flame is removed from under the fiber.
The fiber being close to breaking can either be seen through the microscope or by conducting a transmission measurement.
To ensure the flame stays stable between pulls the image of the camera can be displayed and compared to a reference image taken before the pull. If the flame has changed the pressure p can be adjusted such that the flame matches the reference.
Besides the already mentioned parameters v, t and p the heat and pull method is controllable influenced by the distance between flame and fiber, described by

the height of the torch z. Other influences can not be controlled easily and are therefore sources of error and will be discussed later.

2.2.3 Creating a Fiber Bend

To easily couple into a spatially confined waveguide taper on a chip a bend at the thinnest part of the fiber is introduced.

Method 1: using a different fiber piece as a mold For the mold a stripped fiber is coated in a bit of carbon powder, to prevent the mold sticking to the actual fiber. The tension on the fiber is released,by pushing the fiber holders with the linear stages. Using the gluing stage the mold is pressed against the fiber from below such that a bend forms. Adjust fiber tension and mold height until the bend looks as desired. Engage the flame to relieve the fiber of inner stress by melting it and solidifying in the shape of the bend (annealing).

Method 2: using the flame pressure Using the flame pressure to apply an upwards force on the fiber while the fiber is pushed. The pressure is there to ensure that the bend is upwards with both fibers bending in the same direction and not a S shaped curve. A variation of this method is to push the fiber together first and then use the flame pressure to correct any S shaped bends or bends wich are not orientated upwards.

2.2.4 Characterization of the Pulled Fiber

One characteristic dimension of a pulled fiber is the diameter achieved. This can be measured using a scanning electron microscope, since a visible microscope is not sufficient when the diameter reaches the dimensions of the wavelength of visible light. For this the fiber needs to fit onto the sample holder of the microscope which is difficult to achieve with a continuous fiber. This method is therefore mostly used with small fiber pieces without connectors, glued to a silicon chip. If the fiber is to large to fit, it can be carefully trimmed using pliers.
The second parameter which was measured is the transmission in order to quantify the loss introduced by the procedure. For this a transmission measurement before and after the pull was conducted. From these two measurements the relative loss can be calculated.

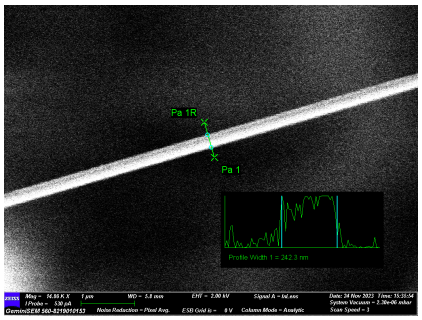

Figure 2.2: SEM picture of a pulled fiber.

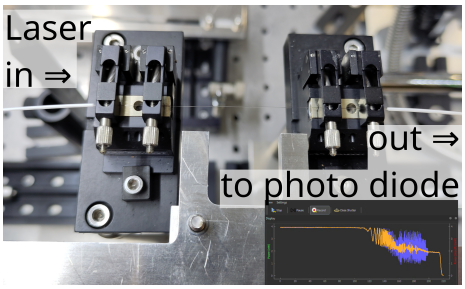

Figure 2.3: Transmission setup.

2.3 Results

2.3.1 Using Pressure to Prevent the Fiber from Bending

Since preliminary tests showed that the cause of fibers breaking was the pressure of the flame, it was hypothesized that a second flame applying the same pressure from the opposite side could prolong the stability of the fiber and yield a longer pull time before the fiber breaks.

To test this, 20 fibers were pulled for the one-flame and the two-flames configuration respectively. The time until the fiber is broken is recorded and plotted as a histogram in figure 2.4. This shows that although the time before a break is, as predicted, prolonged, a much wider range of times is observed. Observing a pull through the microscope gives an explanation: The two colliding flames create turbulence around the fiber which makes it not only less reproducible but also much harder to predict from the visuals at which point the fiber is close to breaking. Due to these reasons, only one torch was used for the following pull experiments.

The pressure exerted from the flow-box mounted above the optical table should have a similar impact on the flame stability. To verify this the flame was kept running for 2 minutes and the video from the camera was analyzed. For each frame a mask was created from all the pixels with a color similar to that of a typical hydrogen flame. The pixels in that mask were counted and the mask added to a cumulative mask. In the end the cumulative mask contains all pixels that were at some point in time part of a mask. The pixel count in the accumulated mask is then used to calculate the amount of flame (pixel count normal mask) in percent of the total observed flame area (pixel count accumulated mask). The result is plotted in figure 2.5. Although it is only a crude method, the plot shows that the flame is the most stable with the flow-box turned off. Consequently the flow-box is turned off for all following experiments.

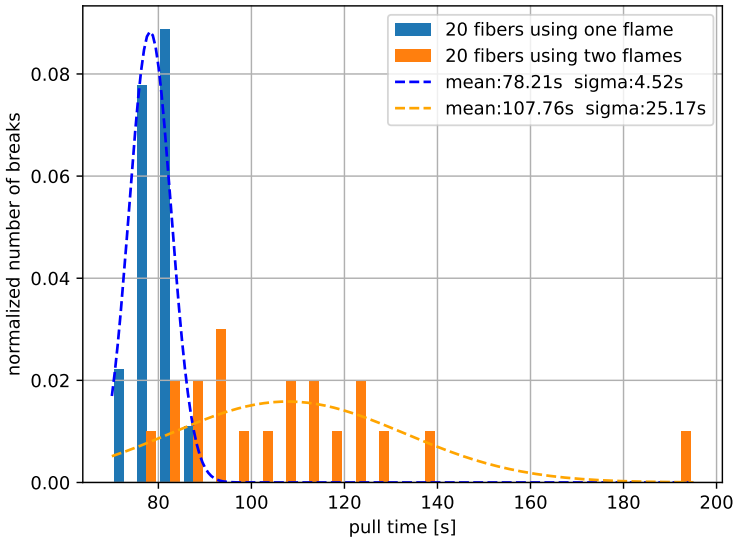

Figure 2.4: histogram of fiber break times using one or two flames with Gaussian fits

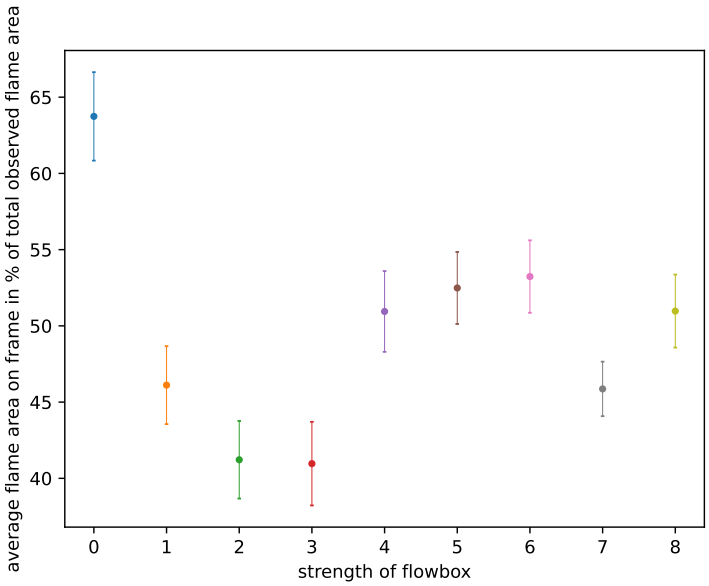

Figure 2.5: Measure of the variability of the flame under different flow-box settings

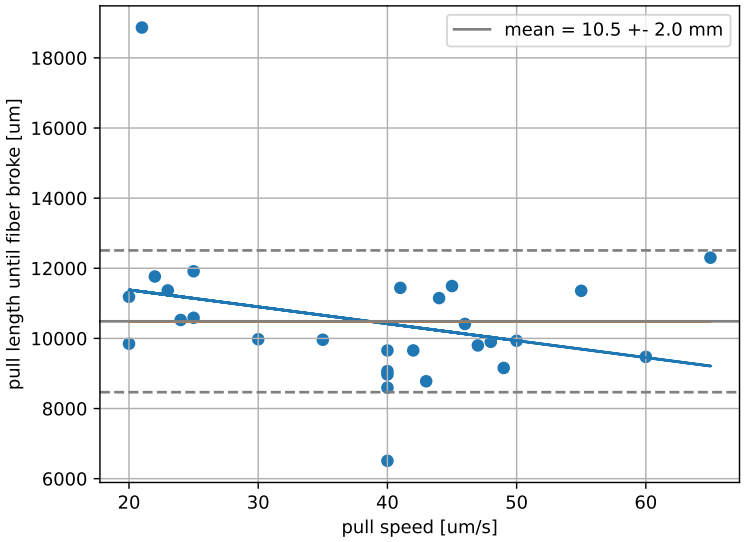

Figure 2.6: break length vs pull speed

2.3.2 Break Time versus Pull Velocity

To examine the dependency on the pull velocity the fiber was pulled until it broke and the break time t_b was recorded. The data of this experiment shows that breaking time declines exponentially with the pull speed. Reparametrization into pull length against pull speed (figure 2.6) should yield a constant, if we expect the fiber to break at a constant diameter. This is due to equation 1.36 being independent of pull speed which means the diameter should be met always at the same pull length. To check if that is the case a likelihood ratio test is performed. For this the data is fitted using the linear model

$$f(v) = m \cdot v + b \tag{2.1}$$

- H_0: $m = 0$; H_1: $m \neq 0$
- Reject the null hypothesis, if the p-value is less then or equal to the significance level $\alpha = 0.01$

The results can be seen in table 2.1; The null Hypothesis is accepted, but it should be noted that the evidence is not very conclusive.

Table 2.1: results of likelihood-ratio test performed on the break time data in figure 2.6

likelihood-ratio λ	28.8%
D Value	2.485
p-value	0.115

2.3.3 Dependency of the Diameter

The smallest diameter achieved depends on the pull length z and hot-zone length L, according to the theory discussed beforehand (compare 1.36), by

$$d(z) = d_0 \exp\left(-\frac{z}{L}\right). \tag{2.2}$$

The achieved diameter can be measured using the SEM and the initial diameter is the fiber diameter 128μm. The three quantities that can be controlled in the experiment are pull speed v, pull time t and pull length z. They are connected by $v = z \cdot t$. This means only one of the three parameters can be kept constant while varying the other two parameters. The hot-zone length L can then be extracted from the data via a fit using a leastsqaures method.

Diameter Study with Constant Pull Speed

With constant pull speed the theory predicts an exponential decrease of the diameter with increasing pull length. This can be seen in the SEM data in figure 2.7. The fit seen in the same picture predicts a hotzone length of $L = 2003 \pm 26\mu$m.

Diameter Study with Constant Pull Time

For constant pull time the theory predicts an exponential decrease of the diameter with increasing pull length. As before, this can be seen in the SEM data in figure 2.8. This time the fit yields $L = 1898 \pm 26\mu$m

Diameter Study with Constant Pull Length

For constant pull length the theory predicts a constant diameter, assuming a constant hotzone. However the SEM data in figure 2.9 shows non constant behavior. The expressed behavior might either be of linear or exponential nature.

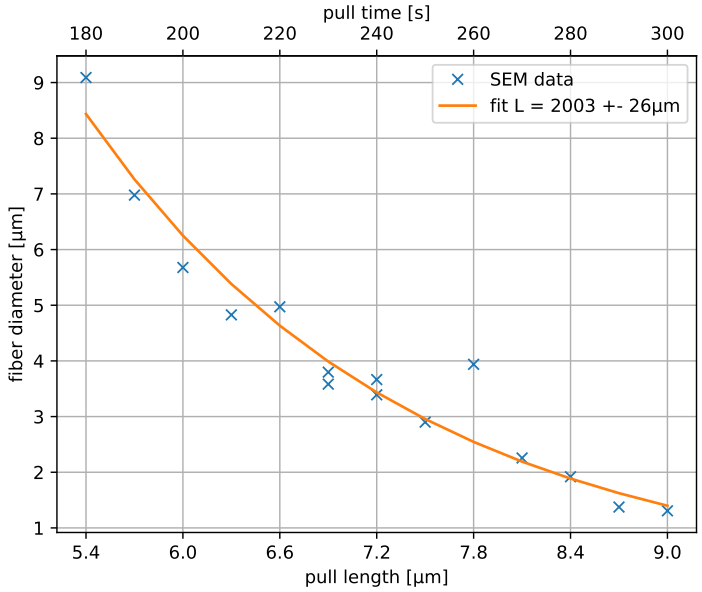

Figure 2.7: smallest diameter of pulled fiber at constant pull speed of $v = 30\mu\text{m/s}$

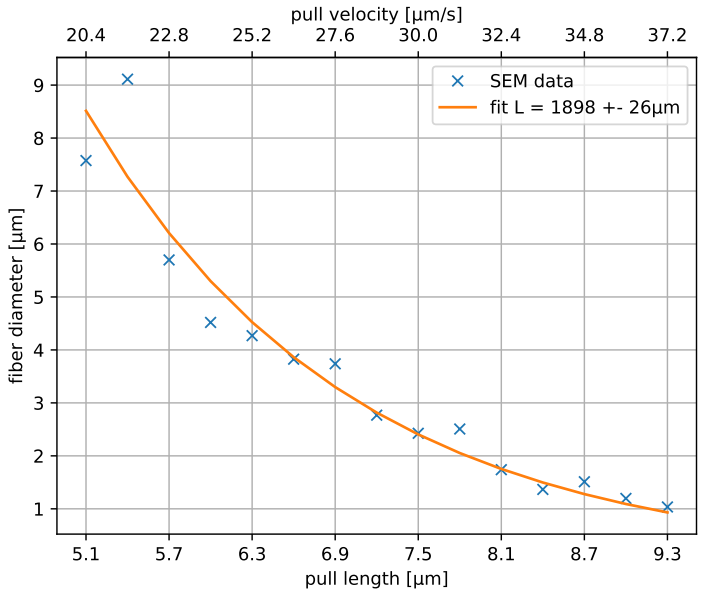

Figure 2.8: smallest diameter of pulled fiber at constant pull time of $t = 250\text{s}$

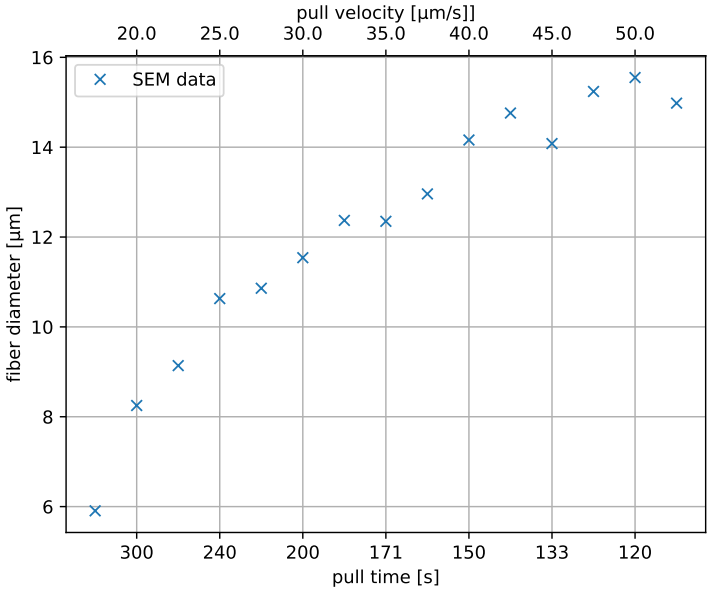

Figure 2.9: smallest diameter of pulled fiber at constant pull length of $z = 6$mm

2.3.4 Transmission Measurements

The transmission displayed in the following is normalized to the absolute transmission of the fiber before the pull. Losses from fiber connectors are thus eliminated.

Typical Transmission Profile

Using the transmission measurement described in section 2.2.4 repeatedly without varying any parameter one can find a typical transmission profile for a pull and how much it differs from pull to pull. The transmission profiles are plotted in figure 2.10. The pull starts at constant 100% relative transmission and slowly transitions into oscillation. The frequency of the oscillation increases with time. During the oscillation the mean transmission decreases. At some point the oscillation stops and the transmission stays constant or decreases slightly at a constant rate. At the point at which the fiber breaks the transmission sharply plummets to 0. Obvious but notable is the variance in the different transmission profiles despite being pulled under the same conditions. From these results an estimate of the error on further transmission measurements can be obtained.

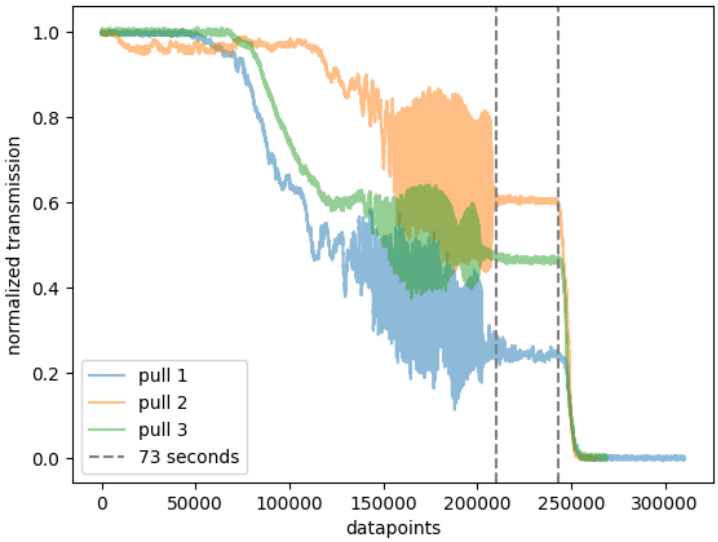

Figure 2.10: Transmission profiles measured under the same condition aligned such that the 0.1 crossing point of the transmission overlaps.

Transmission Profile for Varying Velocity

For different velocities the transmission profile is slightly different as the progression through the various stages of tapering is sped up or slowed down. To be able to align the data-sets the first oscillation is fit to a pre-defined cosine oscillation using a least squares approach. After that the data can be examined. Especially interesting is the time at which the fiber breaks and the time spent in the single mode regime before the brake. The alignment and break time can be seen in figure 2.11.

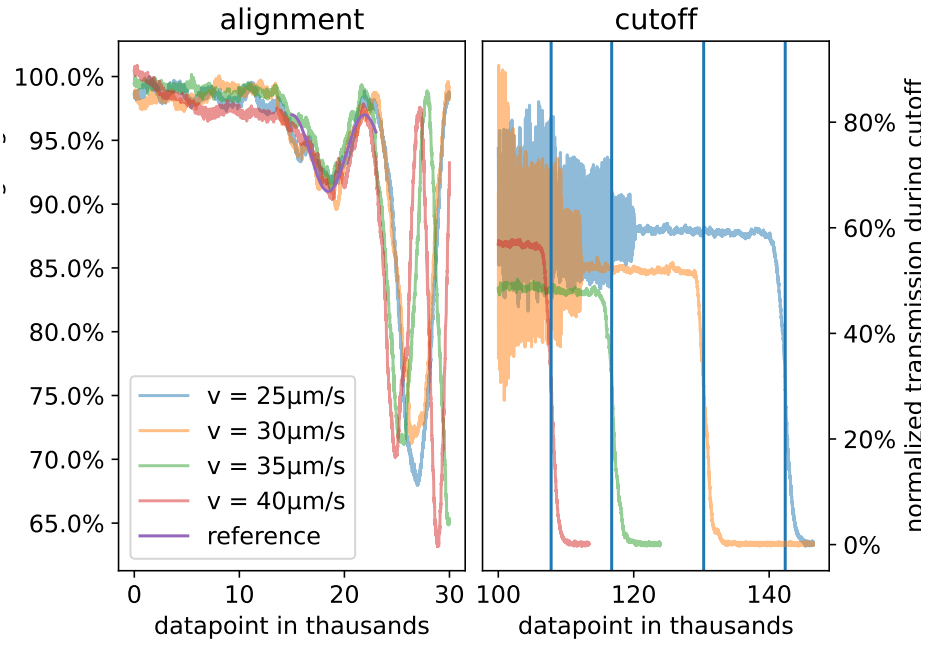

Figure 2.11: Transmission at varying pull velocity. The profiles are aligned in the left plot using a reference function $f(x) = 0.94 + 0.03 \cdot \cos(0.11 \cdot x)$ and in the right plot the break time (crossing point of .3 relative transmission) is evaluated. Note the different transmission axis.

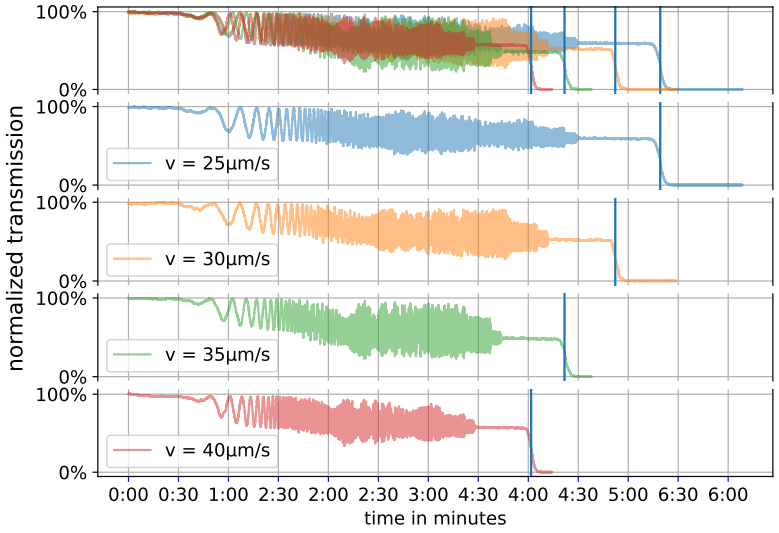

Figure 2.12: Aligned transmission at varying pull velocity.

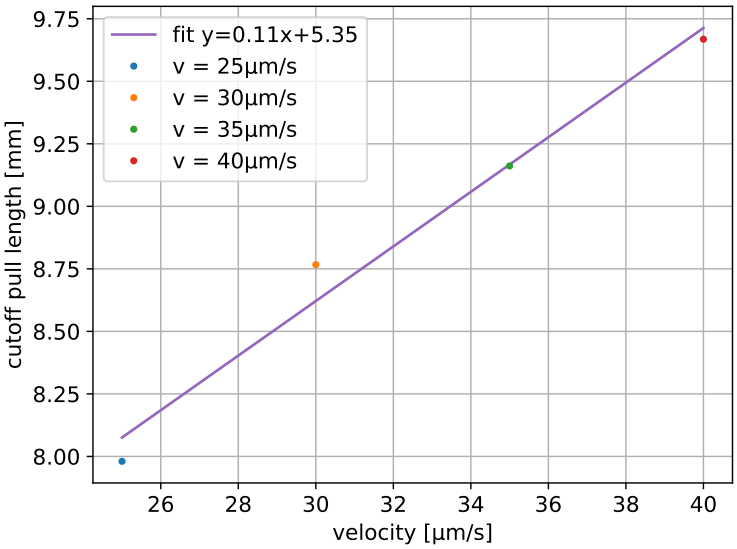

Figure 2.13: Cutoff point in pull length vs the pull velocity

2.3.5 Qualitative Examination of Different Procedures for Creating Fiber-Bends

Different methods for creating a fiber bend were tested qualitatively. The tested methods are using a mold to shape the bend, pushing the fiber together under flame pressure and just pushing the fiber together. As the fiber is so small that it becomes flexible, an annealing step seems to have no considerable impact on bend stability. It might improve transmission as inner stress could lead to losses, but this was not investigated. The process using a mold is time consuming, as considerable setup is required. It does not seem to produce better bends then the other methods used, unless the thinnest part of the fiber is off-center. In that case pushing the fiber often leads to the thinnest part not being on the top of the bend but to one side. Between the pushing with and without flame pressure.

3 | Conclusion and Outlook

3.1 Conclusion

In this thesis a adiabatic mode coupler from optical fiber to on-chip wave-guide was discussed theoretically, simulated and a setup for manufacturing the fiber side of such a coupler build. This heat and pull setup was successfully recreated from [1] and after some familiarization works mostly as expected. In this section the key learnings from that familiarization are summarized and the experimental results compared to the theory discussed. In the end the most optimal procedure steps are given.

Time is not a Good Proxy for the Diameter of the Fiber

Break time measurements for varying pull velocity suggest a constant break-length, but both the SEM data and transmission measurements indicate the opposite. It should be mentioned that this comparison of the different methods only holds under the assumption that fibers break under the flame pressure at a constant diameter.

How to adjust Flame Pressure

To achieve similar flames it does not suffice to set a constant pressure with the pressure gauge used. Rather the pressure is adjusted to produce a flame similar to a picture of a reference flame. Furthermore the flame can be tested and compared to previous flames by pulling fibers and examining notable time stamps such as the start of bending and the time of breaking.

Diameter dependence on pull length

The diameter seems to be well described in dependence of pull length by

$$d(z) = d_0 \exp\left(-\frac{z}{L}\right), \tag{3.1}$$

with hot zone lengths of this setup around 2 mm. The value and error are estimated using the results of the two fits performed. The fits were not provided with errors on the diameter measurement and so their reported error is likely under estimated. The resulting hot-zone lengths $L = 2003 \pm 26\mu$m and $L = 1898 \pm 26\mu$m are (using the error from the fit) significantly different from one another. This is acceptable since the flames used were not completely identical (see Flame Pressure above) and the error is thus estimated higher then the fit

reports.
Not as well established is the diameter dependence on the pull velocity. The theory predicts no dependence but the experiment disagrees. It is hypothesized that with increasing velocity the hot-zone length increases, as the hot fiber does not cool down fast when leaving the hot flame.

$$L \to L_0 + m \cdot v \tag{3.2}$$

If that is the case the hot-zone would increase once the pull starts and could even grow over time if the rate at which the fiber cools is less then the rate of extension of the fiber. However this effect should not be too bad as equation 3.1 seems to hold well for the data with varied pull length.

Procedure

In this segment the procedure which seemed to be repeatable and produced the smallest diameters will be described. Keep in mind that, due to time constraints, the coupling was not tested and therefore no coupling efficiency was measured.

Preparation Prepare some fibers without connectors and one or two with connectors for the calibration step. Prepare any number of fibers with connectors to be tapered down using the pull and push procedure.

Fiber without connectors:

- mechanically cut outer layer at desired length
- pull outer layer away and bend 2nd layer out of the way
- strip outer coating
- strip inner coating
- cut fiber and set aside

Fiber with connectors

- cut fiber with two connectors into two halfs
- strip one of the fibers as described for a fiber without connectors without the last step
- clean the fiber using isopropanol
- Cleave the stripped fiber
- put in the splicer and repeat the last four steps for the other fiber end
- splice and set aside

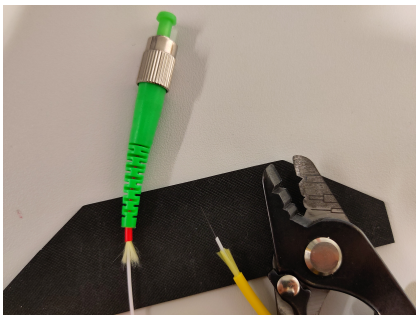

Figure 3.1: strip fiber

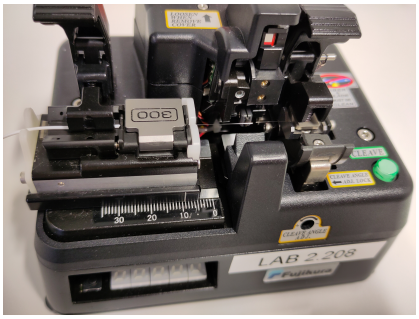

Figure 3.2: cleave fiber

Figure 3.3: splice fiber

Calibration This needs to be done whenever the setup is started to be used after some time off.

- adjust the flame pressure to make the flame fit with reference picture
- engage and disengage the flame a few times. Sometimes this leads to a change in the flame. In this case readjust the flame pressure.
- clean a fiber without connectors using iso-propanol and put it into the setup, heat it up with the flame and pull it. If the fiber does not change in diameter the flame is too weak (more pressure needed) if the fiber bends too early the flame is too strong (less pressure needed). Adjust according to your observations.
- The flame should now be calibrated. Clean a fiber with connectors using iso-propanol and use it to record a reference transmission profile this gives you the time a fiber stays in the single mode regime before breaking.

Figure 3.4: Flame

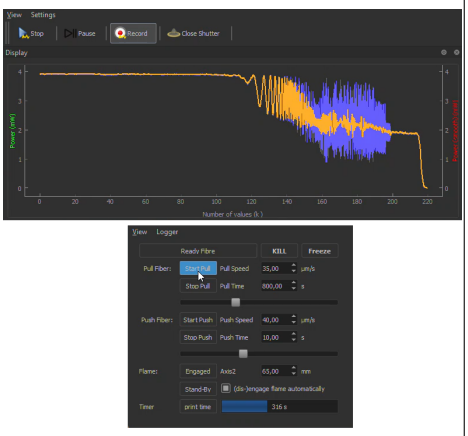

Figure 3.5: Transmission

Push and Pull Execution

- Clean fiber using iso-propanol and put it in the fiber holders
- Engage the flame and wait about a minute for the fiber to melt completely
- Start the pull.
- After the fiber is in the single mode regime for a slightly shorter amount of time than it took the calibration fiber to break, stop the pull.
- disengage the flame and push the fiber until desired bend is achieved.
- briefly engage and disengage the flame to force the bend to go upwards.
- glue the fiber to a holder.

3.2 Outlook

The next step after the heat and pull procedure to be optimized would be the bending procedure. One could examine different bending methods (with flame, pressure, pushing) and minimizing the losses introduced by them. After bending the fiber light could be coupled into on-chip waveguide tapers. Suitable structures would need to be prepared to couple into and measure the coupling efficiency. This could be done in terms of alignment or in terms of the procedures used to prepare the fiber.
Another option would be to challenge the method used in this thesis with different heat sources. This would obviously necessitate changes to the setup. A (CO_2-)laser could be used in heating or the "flame brush" method described by Birks (1992) [25]. In the same paper Birks describes how one would have to vary the hot-zone length in order to achieve an adiabatic taper profile. This could probably be used to further reduce the losses introduced by the tapering procedure, if a different heat source allows for real time manipulation of hot zone length.
To look a bit further into the future, when the method (heat and pull plus bending) is tested to reproducible couple into chips, scalability becomes a concern. How can a closely spaced array of fibers be constructed? The question could maybe be answered either by pulling multiple fibers at once or aligning different pulled fibers on one holder and gluing them in place.

4 References

[1] B. D. Hauer, P. H. Kim, C. Doolin, A. J. MacDonald, H. Ramp, and J. P. Davis, "On-chip cavity optomechanical coupling," *EPJ Techniques and Instrumentation*, vol. 1, no. 1, p. 4, 2014, ISSN: 2195-7045. DOI: 10.1140/epjti4. [Online]. Available: https://doi.org/10.1140/epjti4.

[2] P. Shor, "Algorithms for quantum computation: Discrete logarithms and factoring," in *Proceedings 35th Annual Symposium on Foundations of Computer Science*, 1994, pp. 124–134. DOI: 10.1109/SFCS.1994.365700.

[3] M. Rademacher, J. Millen, and Y. L. Li, "Quantum sensing with nanoparticles for gravimetry: When bigger is better," *Advanced Optical Technologies*, vol. 9, no. 5, pp. 227–239, 2020. DOI: doi:10.1515/aot-2020-0019. [Online]. Available: https://doi.org/10.1515/aot-2020-0019.

[4] L. Childress and R. Hanson, "Diamond nv centers for quantum computing and quantum networks," *MRS Bulletin*, vol. 38, no. 2, 134–138, 2013. DOI: 10.1557/mrs.2013.20.

[5] M. R. Sprague, P. S. Michelberger, T. F. M. Champion, *et al.*, "Broadband single-photon-level memory in a hollow-core photonic crystal fibre," *Nature Photonics*, vol. 8, no. 4, pp. 287–291, 2014, ISSN: 1749-4893. DOI: 10.1038/nphoton.2014.45. [Online]. Available: https://doi.org/10.1038/nphoton.2014.45.

[6] H. J. Kimble, "The quantum internet," *Nature*, vol. 453, no. 7198, pp. 1023–1030, 2008, ISSN: 1476-4687. DOI: 10.1038/nature07127. [Online]. Available: https://doi.org/10.1038/nature07127.

[7] T. E. Northup and R. Blatt, "Quantum information transfer using photons," *Nature Photonics*, vol. 8, no. 5, pp. 356–363, 2014, ISSN: 1749-4893. DOI: 10.1038/nphoton.2014.53. [Online]. Available: https://doi.org/10.1038/nphoton.2014.53.

[8] M. Lončar and A. Faraon, "Quantum photonic networks in diamond," *MRS Bulletin*, vol. 38, no. 2, pp. 144–148, 2013, ISSN: 1938-1425. DOI: 10.1557/mrs.2013.19. [Online]. Available: https://doi.org/10.1557/mrs.2013.19.

[9] K. Srinivasan, P. E. Barclay, O. J. Painter, J. Chen, A. Y. S. Cho, and C. F. Gmachl, "Experimental demonstration of a high quality factor photonic crystal microcavity," *Applied Physics Letters*, vol. 83, pp. 1915–1917, 2003. [Online]. Available: https://api.semanticscholar.org/CorpusID:16054115.

[10] T. Schröder, A. W. Schell, G. Kewes, T. Aichele, and O. Benson, "Fiber-integrated diamond-based single photon source," *Nano Letters*, vol. 11, no. 1, pp. 198–202, 2011, ISSN: 1530-6984. DOI: 10.1021/nl103434r. [Online]. Available: https://doi.org/10.1021/nl103434r.

[11] V. Giovannetti, S. Lloyd, and L. Maccone, "Advances in quantum metrology," *Nature Photonics*, vol. 5, no. 4, pp. 222–229, 2011, ISSN: 1749-4893. DOI: 10.1038/nphoton.2011.35. [Online]. Available: https://doi.org/10.1038/nphoton.2011.35.

[12] M. Smit, K. Williams, and J. van der Tol, "Past, present, and future of InP-based photonic integration," *APL Photonics*, vol. 4, no. 5, p. 050 901, May 2019, ISSN: 2378-0967. DOI: 10.1063/1.5087862. eprint: https://pubs.aip.org/aip/app/article-pdf/doi/10.1063/1.5087862/14010749/050901_1_online.pdf. [Online]. Available: https://doi.org/10.1063/1.5087862.

[13] W. Bogaerts, D. Taillaert, B. Luyssaert, *et al.*, "Basic structures for photonic integrated circuits in silicon-on-insulator," *Opt. Express*, vol. 12, no. 8, pp. 1583–1591, 2004. DOI: 10.1364/OPEX.12.001583. [Online]. Available: https://opg.optica.org/oe/abstract.cfm?URI=oe-12-8-1583.

[14] X. Chen, C. Li, and H. K. Tsang, "Device engineering for silicon photonics," *NPG Asia Materials*, vol. 3, no. 1, pp. 34–40, 2011, ISSN: 1884-4057. DOI: 10.1038/asiamat.2010.194. [Online]. Available: https://doi.org/10.1038/asiamat.2010.194.

[15] D. Taillaert, W. Bogaerts, P. Bienstman, *et al.*, "An out-of-plane grating coupler for efficient butt-coupling between compact planar waveguides and single-mode fibers," *IEEE Journal of Quantum Electronics*, vol. 38, no. 7, pp. 949–955, 2002. DOI: 10.1109/JQE.2002.1017613.

[16] X. Chen, C. Li, and H. K. Tsang, "Fabrication-tolerant waveguide chirped grating coupler for coupling to a perfectly vertical optical fiber," *IEEE Photonics Technology Letters*, vol. 20, no. 23, pp. 1914–1916, 2008. DOI: 10.1109/LPT.2008.2004715.

[17] T. G. Tiecke, K. P. Nayak, J. D. Thompson, *et al.*, "Efficient fiber-optical interface for nanophotonic devices," *Optica*, vol. 2, no. 2, pp. 70–75, 2015. DOI: 10.1364/OPTICA.2.000070. [Online]. Available: https://opg.optica.org/optica/abstract.cfm?URI=optica-2-2-70.

[18] T. Schröder, M. Fujiwara, T. Noda, H.-Q. Zhao, O. Benson, and S. Takeuchi, "A nanodiamond-tapered fiber system with high single-mode coupling efficiency," *Opt. Express*, vol. 20, no. 10, pp. 10 490–10 497, 2012. DOI: 10.1364/OE.20.010490. [Online]. Available: https://opg.optica.org/oe/abstract.cfm?URI=oe-20-10-10490.

[19] D. P. Hampshire, "A derivation of maxwell's equations using the heaviside notation," *Philosophical Transactions of the Royal Society A: Mathematical, Physical and Engineering Sciences*, vol. 376, no. 2134, p. 20 170 447, 2018. DOI: 10.1098/rsta.2017.0447. eprint: https://royalsocietypublishing.org/doi/pdf/10.1098/rsta.2017.0447. [Online]. Available: https://royalsocietypublishing.org/doi/abs/10.1098/rsta.2017.0447.

[20] W. Demtröder, *Electrodynamics and Optics*. 2019, p. 449, ISBN: 978-3-030-02289-1. DOI: https://doi.org/10.1007/978-3-030-02291-4.

[21] T. Walsh, *OPhysics — ophysics.com*, https://ophysics.com/t2.html, [Accessed 23-06-2024].

[22] L. Novotny, "Strong coupling, energy splitting, and level crossings: A classical perspective," *American Journal of Physics*, vol. 78, no. 11, pp. 1199–1202, Nov. 2010, ISSN: 0002-9505. DOI: 10.1119/1.3471177. eprint: https://pubs.aip.org/aapt/ajp/article-pdf/78/11/1199/13132946/1199_1_online.pdf. [Online]. Available: https://doi.org/10.1119/1.3471177.

[23] W. Demtröder, *Experimental Physik 1 - Mechanik und Wärme*. 2021, p. 511, ISBN: 978-3-662-62727-3. DOI: https://doi.org/10.1007/978-3-662-62728-0.

[24] P. P. Cappellaro, *22.51 Quantum Theory of Radiation Interactions: Complete Course Notes | Quantum Theory of Radiation Interactions | Nuclear Science and Engineering | MIT OpenCourseWare — ocw.mit.edu*, https://ocw.mit.edu/courses/22-51-quantum-theory-of-radiation-interactions-fall-2012/resources/mit22_51f12_notes/, [Accessed 13-06-2024], 2012.

[25] T. Birks and Y. Li, "The shape of fiber tapers," *Journal of Lightwave Technology*, vol. 10, no. 4, pp. 432–438, 1992. DOI: 10.1109/50.134196.

[26] A. Taflove, S. C. Hagness, and M. Piket-May, "9 - computational electromagnetics: The finite-difference time-domain method," in *The Electrical Engineering Handbook*, W.-K. CHEN, Ed., Burlington: Academic Press, 2005, pp. 629–670, ISBN: 978-0-12-170960-0. DOI: https://doi.org/10.1016/B978-012170960-0/50046-3. [Online]. Available: https://www.sciencedirect.com/science/article/pii/B9780121709600500463.

[27] M. J. Burek, Y. Chu, M. S. Z. Liddy, *et al.*, "High quality-factor optical nanocavities in bulk single-crystal diamond," *Nature Communications*, vol. 5, no. 1, p. 5718, 2014, ISSN: 2041-1723. DOI: 10.1038/ncomms6718. [Online]. Available: https://doi.org/10.1038/ncomms6718.

[28] D. E. Stewart, *Numerical Analysis: A Graduate Course*. 2022, pp. XV, 632, ISBN: 978-3-031-08120-0. DOI: https://doi.org/10.1007/978-3-031-08121-7.

[29] *COMSOLMultiphysics® Software*, https://www.comsol.com/comsol-multiphysics, Accessed 12-05-2024, version 5.6 (build: 280).

[30] *Ansys Lumerical FDTD | Simulation for Photonic Components*, https://www.ansys.com/products/optics/fdtd, Accessed 12-05-2024, release 2020 R2.4, version 8.24.2502.

Acknowledgements

First and foremost I am deeply grateful to Professor Wolfram Pernice for giving me the opportunity to work in his research group for my thesis.
My gratitude exceeds to Mark Ulanov for his guidance, valuable insights and patience. A special thanks for the images and measurements done by him with the electron microscope.
I would also like to mention and thank the guys at the workshop for quickly machining the various parts and iterations thereof necessary for the setup.
Finally, I want to thank the members of the Neuromorphic Quantumphotonics group, for their feedback during (sub-)group meetings, help with the simulations and insight into their work.

Erklärung

Ich versichere, dass ich diese Arbeit selbstständig verfasst und keine anderen als die angegebenen Quellen und Hilfsmittel benutzt habe.

Heidelberg, den 8.7.24, 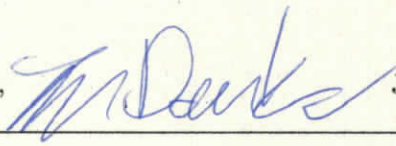 Jan Dumke

5 | Appendix

Here are most of the connecting pieces that were manufactured out of Aluminum for the setup.

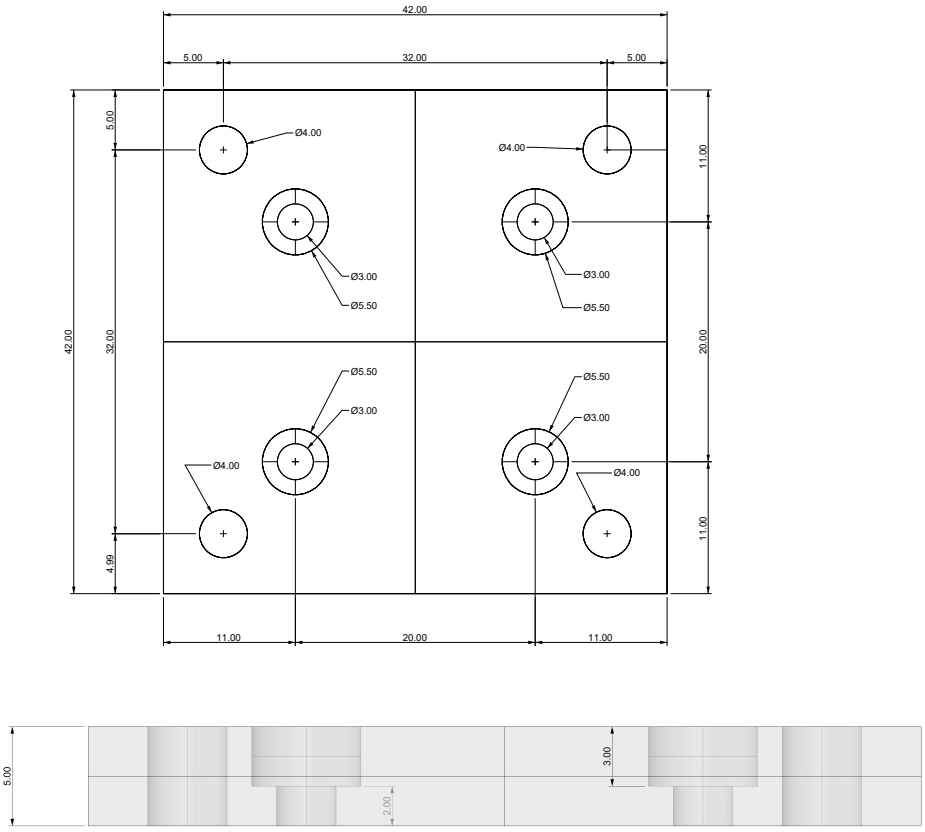

Figure 5.1: Connector in the torch holder moving setup connecting the motorized linear-stage to the angle bracket

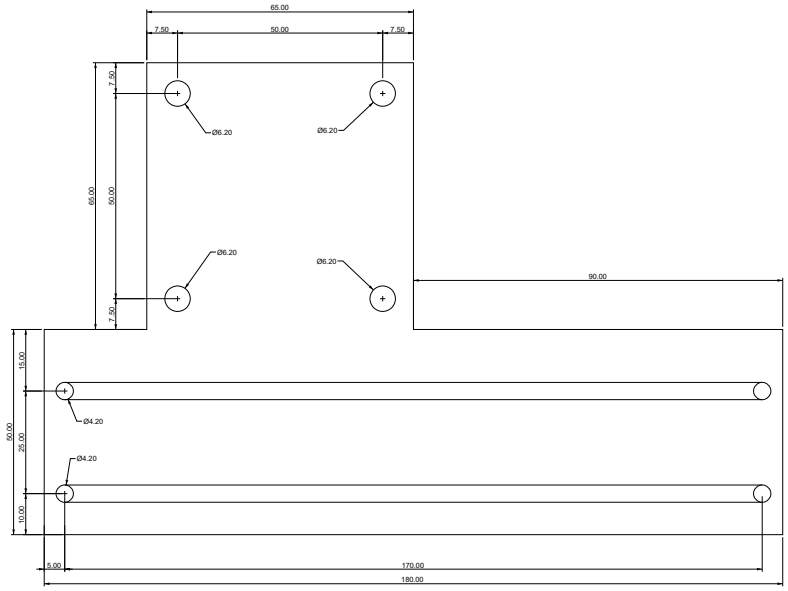

Figure 5.2: Connector in the torch holder connecting the clamps to the manual linear stage

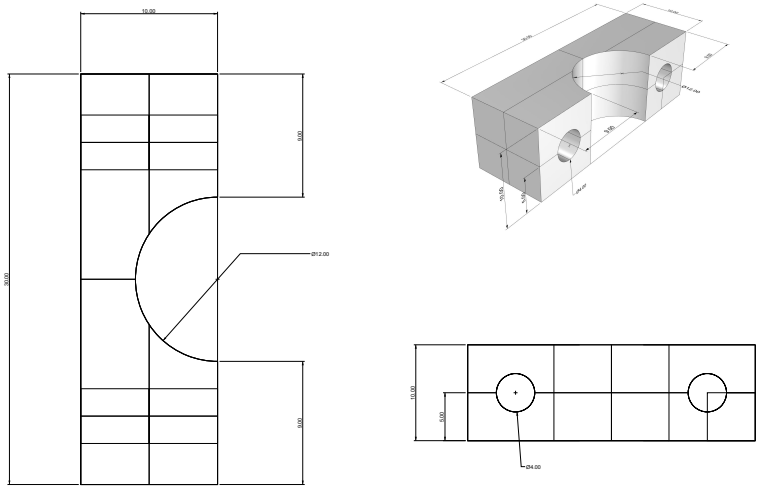

Figure 5.3: Clamps holding the hydrogen torch. 4 are needed.

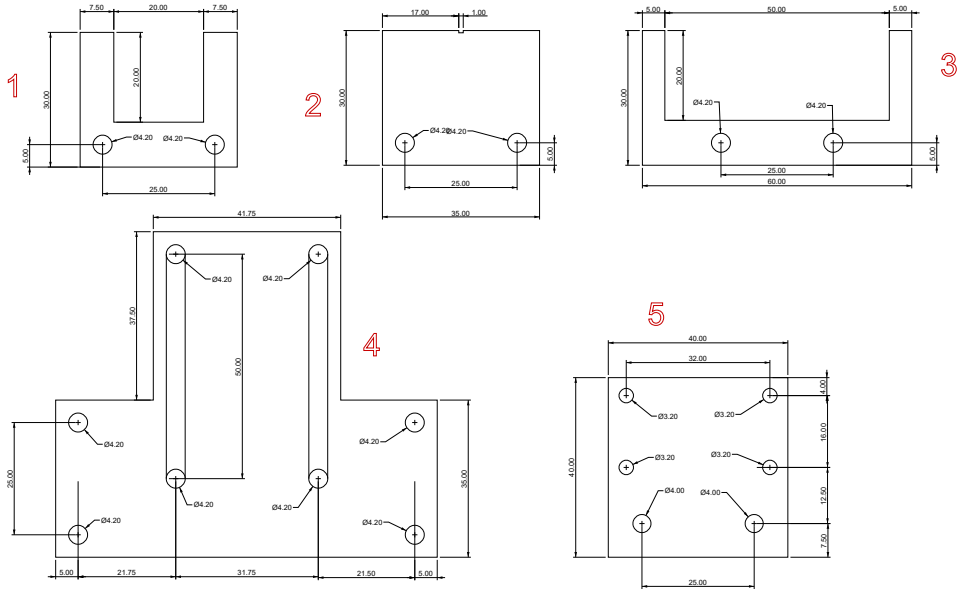

Figure 5.4: Various parts for the gluing stage. 1) fiber holder a fiber can be glued to. 2) either used to hold a chip onto which the fiber is to be glued or holds a mold to introduce a bend in a fiber. 3) like 1) but bigger. 4) connects optical posts to the xy stage 5) connects the xy stage to the z stage.